Origami derived self-assembly stents fabricated via 4D printing

Wei Zhao [a], Nan Li [a], Liwu Liu [a], Jinsong Leng [b], Yanju Liu [a],[*]

[a] Department of Astronautical Science and Mechanics, Harbin Institute of Technology (HIT), P.O. Box 301, No. 92 West Dazhi Street, Harbin 150001, People's Republic of China
[b] Center for Composite Materials and Structures, Harbin Institute of Technology (HIT), P.O. Box 3011, No. 2 YiKuang Street, Harbin 150080, People's Republic of China

ARTICLE INFO

ABSTRACT

Researches on self-assembly stents are expanding owing to the development of manufacturing technology and advanced materials. Many design strategies have been developed to obtain stents with large shrinkage ratios that facilitate minimally invasive implantation. The design of self-assembly stents that use the origami concept to achieve large shrinkage ratios is expected to introduce new opportunities in the treatment of tracheal diseases or vascular stenosis. Depending on the shape and angle of the unit cells, stents with different shrinkage ratios can be obtained by adjusting the geometric parameters and arranging them periodically. Further, the helical angle is introduced, and the effect on the shrinkage ratios of stents is investigated. Moreover, the lightweight design is presumed to increase structural flexibility and further improve the shrinkage ratio. Self-assembly stents with different unit cells are prepared via 4D printing, and the widespread application is illustrated by comparing experimental and theoretical studies. Furthermore, potential biomedical applications of self-assembly stents with large shrinkage ratios and deployable functions are suggested with demonstrative examples.

1. Introduction

Stents are commonly used in minimally invasive interventional therapy [1,2]. Compared with traditional medical techniques, minimally invasive interventional therapy has advantages such as less trauma and higher safety, which greatly reduces the operation difficulty and alleviates the pain of patients. Most of the stents are woven from alloy wires, remaining in the body permanently. However, there are risks for the second surgery. Consequently, stents made of biodegradable materials have been paid more and more attention to avoid the complications caused by the metal stents. Since minimally invasive interventional therapy needs to select a vein or superficial artery approach that is easy to puncture, the stent must have excellent contractility to be delivered to the lesion location through complicated tortuous vessels.

To obtain a stent with a large shrinkage ratio and facilitate minimally invasive implantation, one promising technology is origami. Utilizing origami technology [3], the two-dimensional structure can be folded into three-dimensional structures, which has a wide range of applications with its advantages of light weight, rapid manufacturing, customization and other advantages. Origami-derived structures exhibit high flexibility, as their properties are coupled with a dynamic change in folding patterns [4–7]. There are four main origami design approaches,

namely origami tessellations, origami structure based on tucking molecules, curved-crease origami, and origami structure based on concentric pleating. Several tessellations are well known among origami artists and scientists, such as Waterbomb, Miura-ori. Furthermore, Ron Resch et al. [8,9] developed other origami tessellations to create origami-based mechanical metamaterials [10] or freeform surface approximations [11]. These kind of structures can switch from one configuration to another by folding along the designed creases, and the mechanical properties of an origami structure are mainly determined by its folding deformation mode.

Origami-derived structures exhibit high flexibility, as their properties are coupled with a dynamic change in folding patterns. This kind of structure can switch from one configuration to another by folding along the designed creases, and the mechanical properties of an origami structure are mainly determined by its folding deformation mode. For example, waterbomb origami tube is a tubular origami structure with complex folding behavior, which consists of two mountain and four valley creases [12,13]. Waterbomb is a bistable mechanism, meaning that it has two stable equilibria, and utilizing this mechanism the waterbomb-based stent can change from one stable configuration to the other [14]. Utilizing this function, the origami design philosophy can be used to improve medical devices [15].
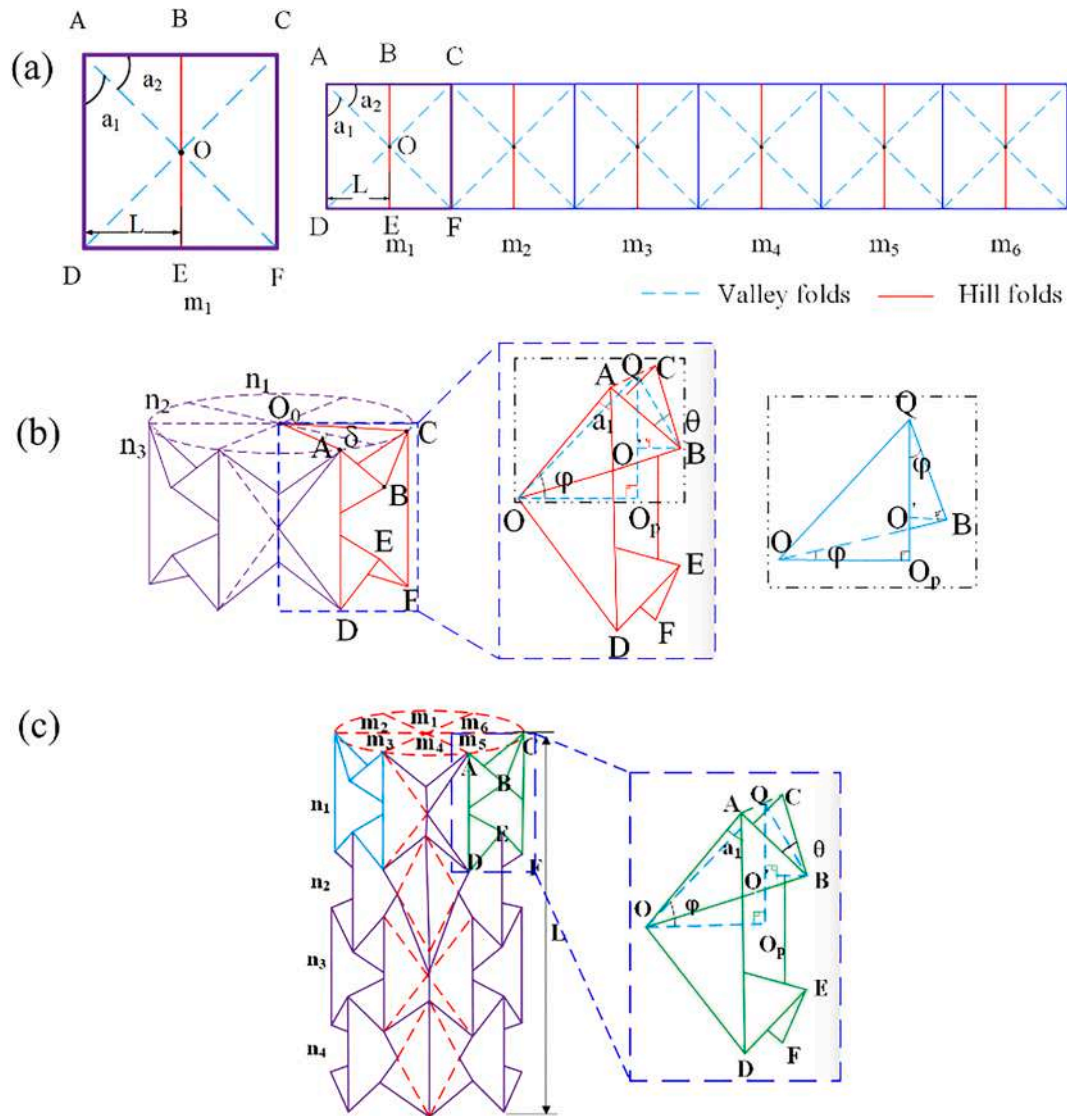

Fig. 1. (a) Design of the unit cell and folding pattern of the stent (b) Schematic of a stent with a single layer (c) Perspective of a stent with four rows, an intermediate state in the folding process and a schematic diagram of a unit cell in the folding process.

In general, origami structures have a complex configuration, making them difficult to fabricate. However, the development of four-dimensional (4D) printing technology makes such fabrication possible. Take shape memory polymer (SMP) [16] as raw material for 4D printing [17–19], the shape and performance of 4D printed structures can respond to the environment under external stimuli, such as heat [20–22], light [23], water [24] and magnetic fields [25], which have been widely used in biomedical applications [26–28]. Recent advances in self-folding technologies [29–31] could be of particular interest for the development of novel minimally invasive procedures, while the applicability of optimized 3D assembly methods based on bending, curving, and folding have also been investigated [32]. For minimally invasive surgery, origami-derived medical devices fabricated by 4D printing are endowed with the self-assembly property, which can be inserted into the body through a compact small incision to reach areas that are otherwise inaccessible and deployed in their working state at the destination. The 4D printed biomedical devices show a series of functional characteristics such as self-adaptation and self-assembly, showing great application potential and practical value in the biomedical field.

Numerous studies have been performed on the self-assembly and recovery behavior of 4D-printed structures. For example, the active composite developed by Ge et al. was precisely printed in an elastic matrix with shape-memory polymer (SMP)-based fibers and used as intelligent movable hinges to realize the self-assembly function of origami [33]. Bobbert et al. proposed a novel origami-based design to repair vertebral compression fractures [34]. Banerjee et al. proposed an origami-based deployable surgical retractor with the aim to improve the interaction between instruments and tissues in face-lift operations [35]. Sargent et al. proposed an origami-based system (OriGuide) to optimize the ex vivo support for the insertion of flexible instruments in RAS [36]. Felton et al. [37] developed a self-folding crawling robot by using a shape-memory composite that could recreate the basic folding pattern by using a hinge fabricated via SMP. Teoh et al. [38] performed a preliminary study on the effects of the hinge axis and hinge thickness on the recovery behavior of 4D-printed origami structures. Liu et al. [39] utilized non-focused light to realize the self-folding of polymer films. A predefined ink region (i.e., hinges) can realize both relaxation and contraction to fold a flat sheet into a 3D object. Furthermore, Tolley et al. [40] presented a self-assembly origami structure composed of a shape-memory composite that could be activated in a uniformly heated oven. Cube, icosahedron, flower, and Miura-pattern structures could be deployed in the oven in 4 min.

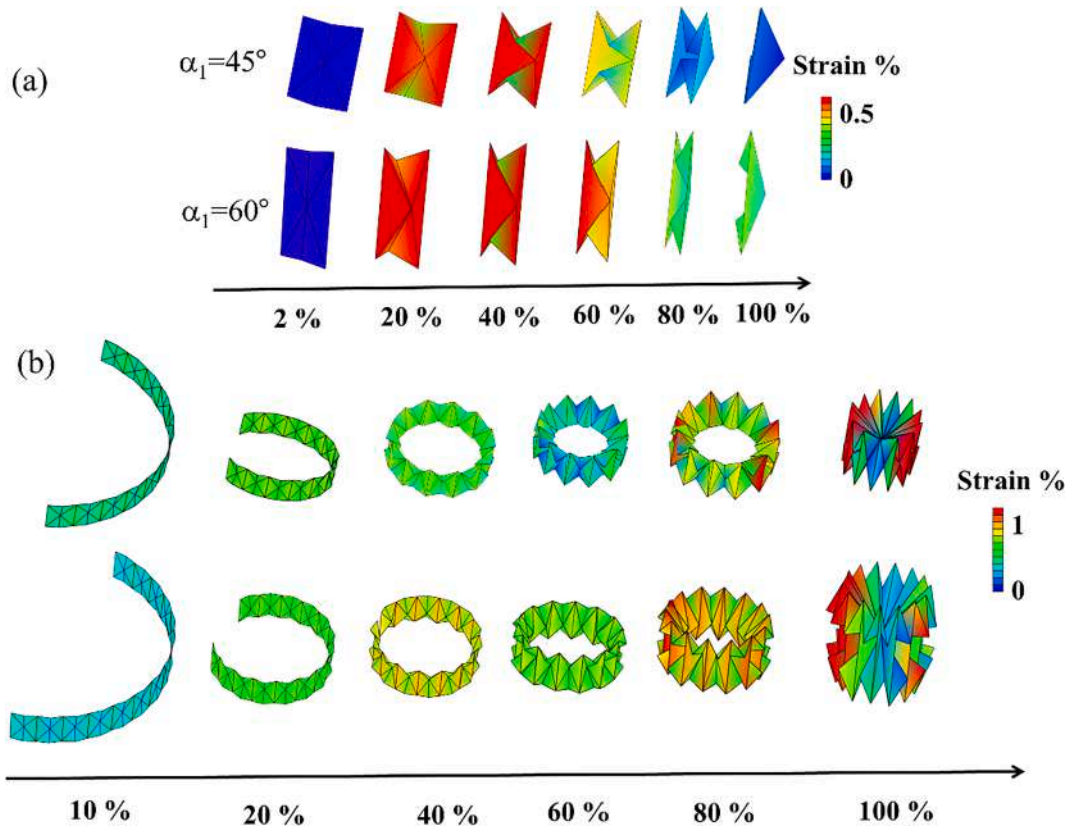In this study, origami-derived self-assembly stents were proposed

Fig. 2. Folding process of (a) unit cell with $\alpha_1 = 45°$ and $\alpha_1 = 60°$ and (b) the stent with only one layer.

and demonstrated. Combined with 4D printing, stents were fabricated and can be folded into small shapes along predesigned creases to complete the self-assembly process stimulated by heat. The final states of the folded stent depend largely on the geometric parameters of the unit cell. The relationship between the geometric construction and the shrinkage ratio was deduced, and the design strategy to obtain the maximum contraction value was proposed. The introduction of a lightweight design not only changed the geometric parameters of the flexure hinge but also improved the flexibility of the structure, along with the shrinkage ratio. These results provided a new approach to fabricate self-assembly stents for minimally invasive interventional therapy.

2. Design of the stents

One of the most interesting features of origami-derived structures is the folding pattern that enables the stent to fold and unfold longitudinally and radially. The length and diameter of the stent decrease during folding and increase during expansion. In the folding process, subunits bounded by creases are introduced in the structure, increasing its flexibility. These creases enable the stents packed compactly and exhibited flexibility during folding. Using the folding method instead of a more complex joining mechanism enables the structure to contract and expand smoothly without tangles or fractures.

For the stents, the folding process was achieved by dividing the structure into a series of collapsible elements. According to pre-designed creases, the stent can be folded and shrunk into a smaller structure. Exemplified by a stent composed of one layer unit-cell, the design prototype of the unit cell and the folding pattern is shown in Fig. 1 (a) and (b).

The design of the unit cell is illustrated in Fig. 1(a), where the dotted lines represent creases and point "O" is the center of the fold. In the folding process, the dashed line will fold down when applying downward pressure on point "O". In the newly formed stent structure, the

dashed part concaved downward is called "valley folds" while the solid lines form the periphery of the new structure and are called "hill folds". The plane expansion diagram of the collapsible stent is presented in Fig. 1(b), which is composed of six rectangular elements (m_1, m_2, m_3, m_4, m_5, m_6). The unit cells are connected end by end and arranged periodically, where AD edge in unit m_1 and C′F′ edge in unit m_6 are connected to form a stent. Fig. 1(c) illustrates the schematic diagram of the self-assembly stent with four rows in the folding process.

When the stent is fully folded, it satisfies the geometric relationship of $R_{o1} = R_{o2} = OB$. The length of OB is directly related to the shrinkage ratio of the structure. By controlling the angles α_1 and α_2, the lengths R_{o1} and R_{o2} can be adjusted, and the folded shape of the stent can be controlled. According to the geometry relation, the radii during the folding process can be given by:

$$R_{o1} = \frac{l\sin\theta}{\tan\delta} + l\cos\theta\frac{\cos^2\alpha_1 - \sin^2\alpha_1\cos^2\theta}{1 - \sin^2\theta\sin^2\alpha}, R_{o2} = \frac{AC/2}{\sin\delta} = \frac{l\sin\theta}{\sin\delta} \tag{1}$$

When the stent is completely folded, it satisfied the relation of $R_{o1} = R_{o2} = OB$ (Note, Supporting Information S1). And the overall length "L" of the stent during the folding process can be further expressed as:

$$L = n\frac{2l}{\tan\alpha_1} - (n-1)\frac{l\sin2\alpha_1\cos^2\theta}{1 - \sin^2\alpha_1\sin^2\theta} \tag{2}$$

The layout of the unit cell has an obvious effect on the shrinkage ratio of the whole stent. For the stent to achieve its maximum shrinkage ratio and be fabricated as a compact package, the critical design includes (a) folding along the radial direction to minimize the radius and (b) folding along the axis to minimize the length. When the structure is completely folded, the side OB is the radius of the structure, and BC is parallel to edge AD. The lengths of BC and AD directly affect the shrinkage ratio. When AC = AD, i.e., $L_1 = L_3$, the geometrical relationship of $2O_0B = AD$ is satisfied after complete folding, and the maximum
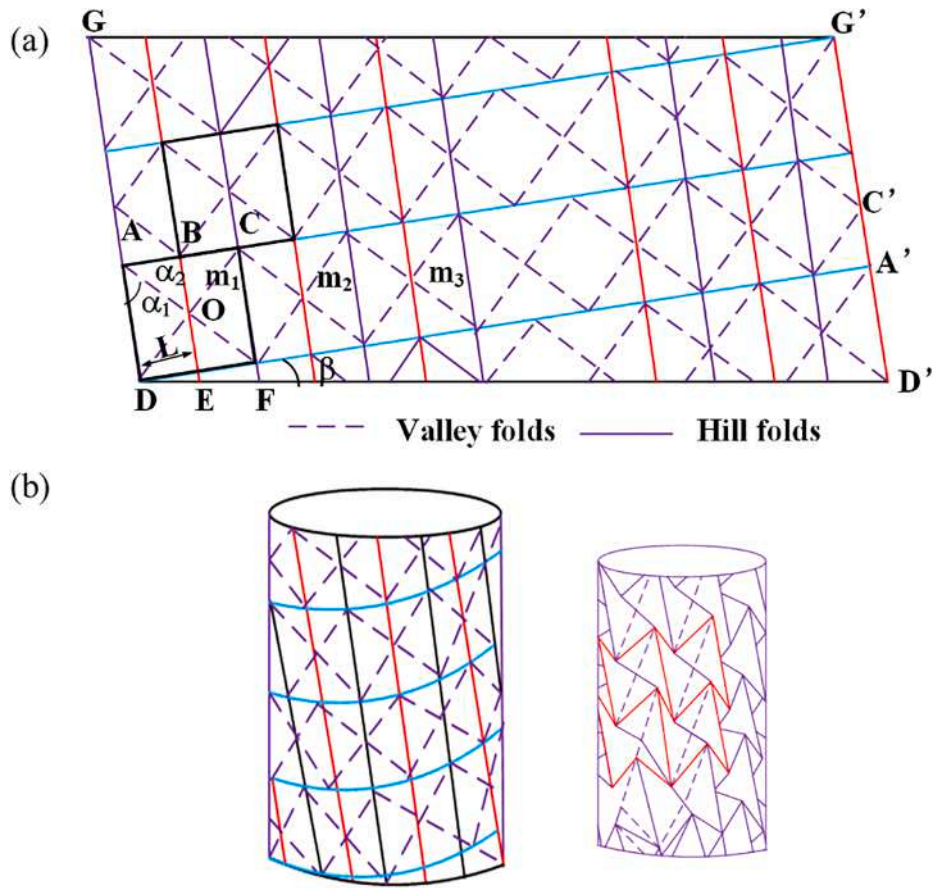
Fig. 3. The schematic diagram of the stent with a helical angle (a) Design of the creases and folding pattern (b) Schematic diagram of the stent before folding (c) schematic diagram of the stent in the folding state.
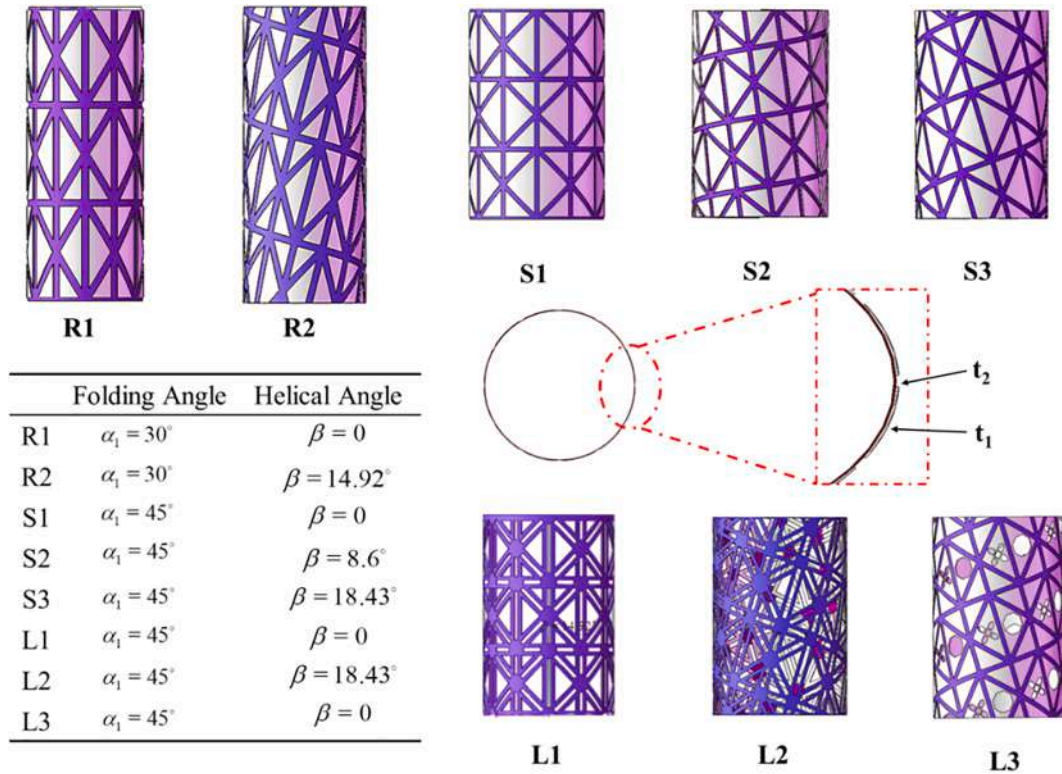

	Folding Angle	Helical Angle
R1	$\alpha_1 = 30°$	$\beta = 0$
R2	$\alpha_1 = 30°$	$\beta = 14.92°$
S1	$\alpha_1 = 45°$	$\beta = 0$
S2	$\alpha_1 = 45°$	$\beta = 8.6°$
S3	$\alpha_1 = 45°$	$\beta = 18.43°$
L1	$\alpha_1 = 45°$	$\beta = 0$
L2	$\alpha_1 = 45°$	$\beta = 18.43°$
L3	$\alpha_1 = 45°$	$\beta = 0$

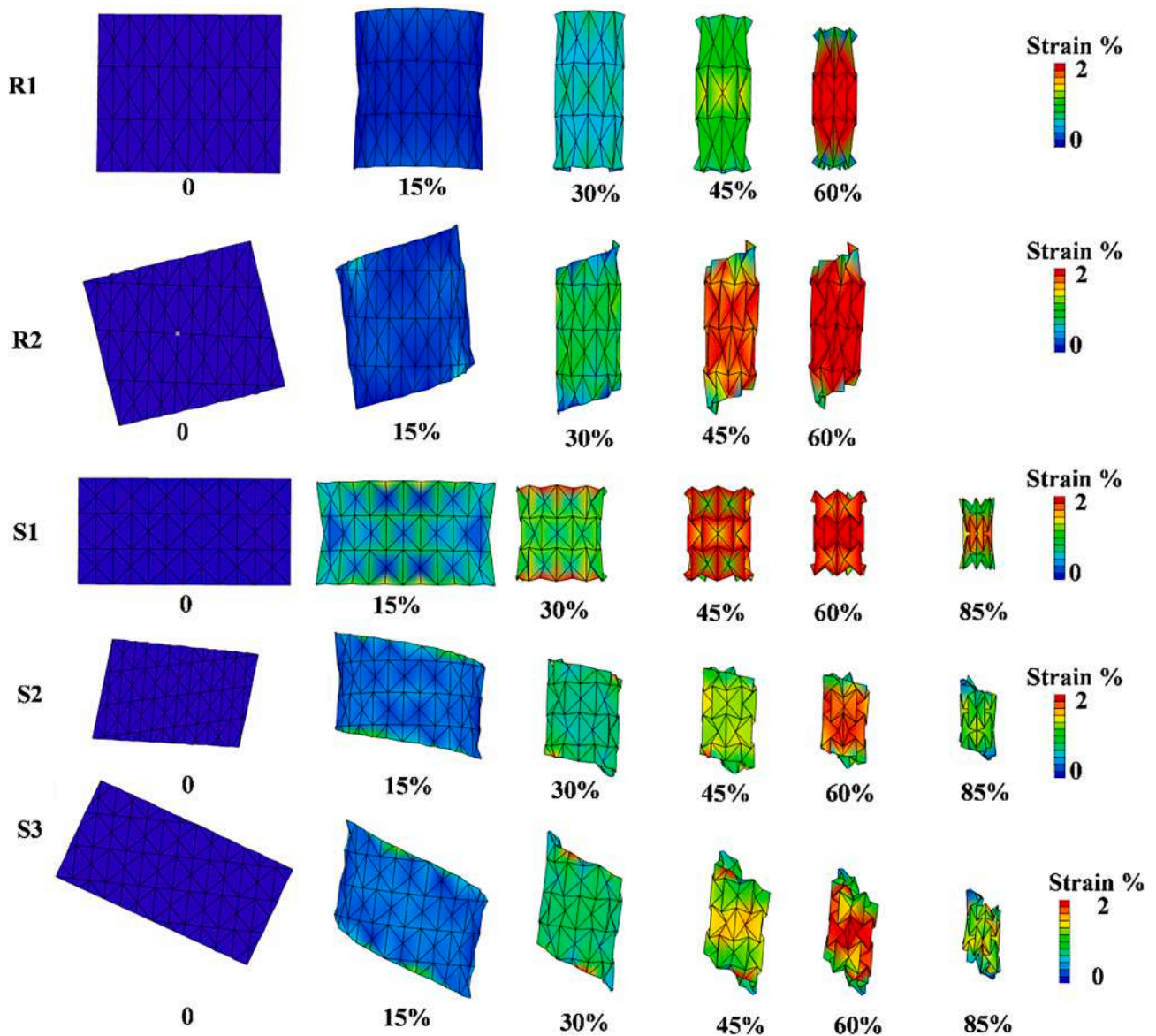**Fig. 4.** Design of stents R1, R2, S1, S2, S3, L1, L2 and L3.

Fig. 5. Simulation of the folding process of the stents R1, R2, S1, S2 and S3.

shrinkage ratio is attained (Note: Supporting Information, Fig. S1).

For the square element, $\alpha_1 = \alpha_2 = 45°$ and the sides are of equal length, which satisfies the geometrical relationship of 2AB = AD. After folded, the sides of AB, AE and DE are at the outermost end of the radial direction and are parallel to each other (Note: Supporting Information, Fig. S2). For the stent composed of square elements, the most harmonious deformation can be obtained in the folding process, i.e., AB + DE = AD. Compared with stents composed of elements having other geometrical parameters, the vertical shrinkage ratio is maximized under this design condition without a spiral angle. The folding processes of the unit cell with $\alpha_1 = 45°$ and $\alpha_1 = 60°$ are illustrated in Fig. 2 (a). The folding processes of the stent with only one layer of the unit cell with $\alpha_1 = 45°$ and $\alpha_1 = 60°$ are illustrated in Fig. 2 (b), respectively. It can be seen that the unit cell with $\alpha_1 = 60°$ exists the phenomenon of deformation mismatch due to the unequal length of the side.

Furthermore, the introduction of a helical angle further increases the shrinkage ratio along with the length and radial directions. The introduction of a helical angle enables the structure to be twisted, making the contraction more compact and increasing its shrinkage ratio. With the introduction of a helical angle, the layout of the unit changes, and the unit cells that are previously aligned horizontally are tilted upward at an

angle of β. Although the structure is composed of three complete rows of elements, the introduction of a helical angle splits one row of elements into two rows n_3 and n_3', forming a complete element as shown in Fig. 3. Furthermore, to connect the structure, another half unit cell m_7 is introduced in the array and arranged horizontally. The elements differ by half a cell in the arrangement of each column. For example, the elements of n_1 and n_3 arranged along the direction of the spiral angle are staggered by half a cell with respect to the elements arranged in row n_2.

According to the geometrical relation, the helical angle β can be expressed as:

$$\beta = \arctan\left[\frac{2\tan(\alpha_1 + \alpha_2)\cos^2\alpha_1 - \sin\alpha_1\cos\alpha_1 + \sin^2\alpha_1\tan\alpha_1\cos^2\theta}{(2m+1)\sin\theta\tan\alpha_1\tan(\alpha_1 + \alpha_2)(1 - \sin^2\alpha_1\sin^2\theta)}\right] \quad (3)$$

The radius of the stent in the first folding process can be expressed as:

$$R_{o1} = \frac{l\sin\theta\cos\beta}{\tan\delta} + l\cos\theta\frac{\cos^2\alpha_1 - \sin^2\alpha_1\cos^2\theta}{1 - \sin^2\theta\sin^2\alpha} \\ - \frac{l}{\tan(\alpha_1 + \alpha_2)}\frac{\sin2\alpha_1\cos\theta}{1 - \sin^2\theta\sin^2\alpha_1} \quad (4)$$

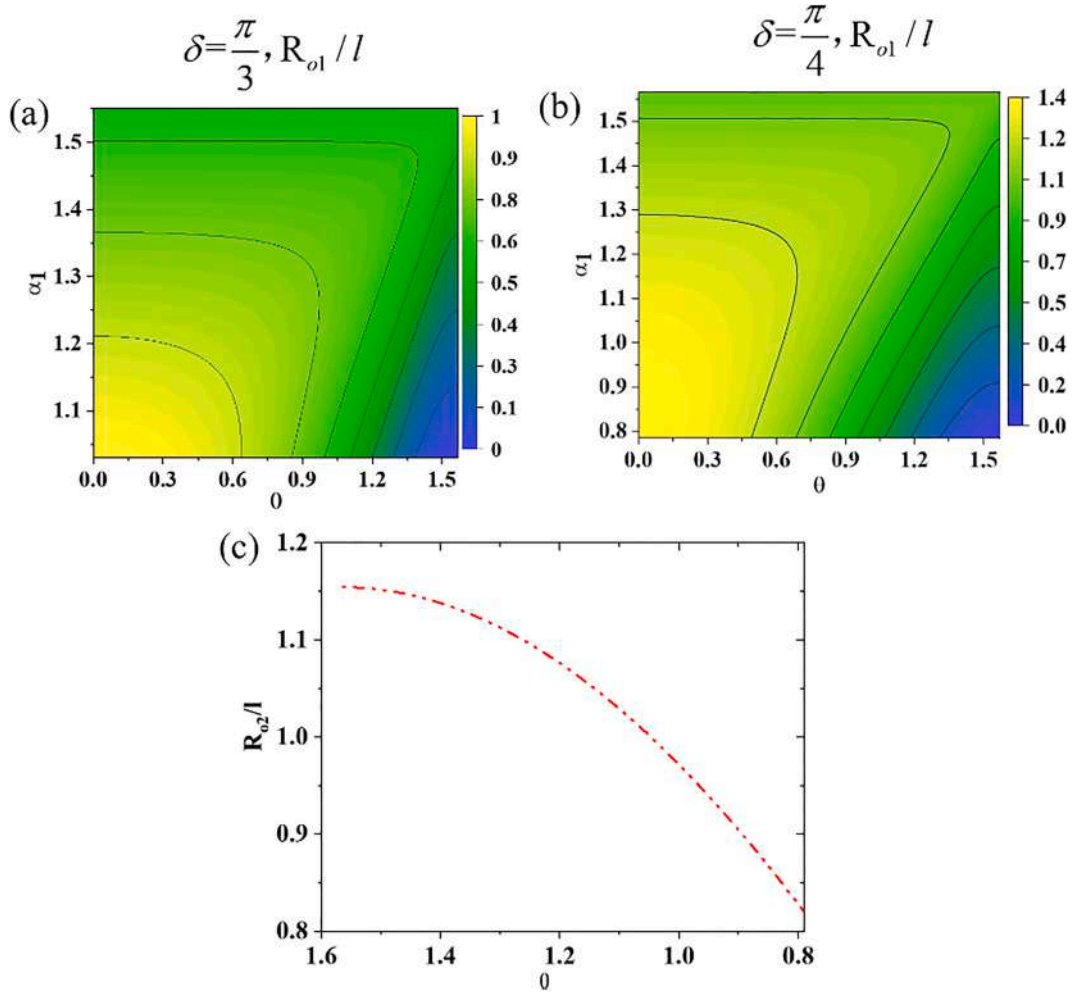Moreover, according to the geometrical definition, the radius in the

Fig. 6. Theory results of R_{o1}/l and R_{o2}/l changing with θ during the folding process (a) $\delta = \frac{\pi}{3}$ (b) $\delta = \frac{\pi}{4}$ (c) R_{o2}/l changing with θ.

second step can be expressed as:

$$R_{o2} = \frac{AC/2}{\sin\delta} = \frac{l\sin\theta\cos\beta}{\sin\delta} \tag{5}$$

The overall length of the structure during the folding process can be expressed as:

$$L = \left(n\frac{2l}{\tan\alpha_1} - (n-1)\frac{l\sin2\alpha_1\cos^2\theta}{1 - \sin^2\alpha_1\sin^2\theta} \right)\cos\beta \tag{6}$$

In this work, we designed eight types of stents (Fig. 4): R1 (rectangular units without helical), R2 (rectangular units with helical), S1 (square elements without helical), S2 (square elements with helical), S3 (square elements with helical), L1, L2 and L3 (lightweight design), respectively (Design details can be found in Supporting Information, S3). It is worth mentioning that the objective of the lightweight design is to achieve maximum efficiency with minimum consumption. The introduction of the lightweight design is expected to improve the flexibility of the stent by reducing the amount of material used. The origami structure based on the SMP can fulfill its self-assembly function using the unique driving mechanism of the SMP-based flexible hinge. For the stents without helical, 6 elements are spiraling into a circle to form one layer, while 6.5 elements for the stents with helical. In this study, a helical angle of $\beta = 14.92°$ is introduced into the cylindrical structure composed of a rectangular element. With an increase in the helical angle β, the shrinkage ratio along the length and radius increases gradually. Two different helical angles-$\beta_1 = 8.6°$ (denoted as S2) and $\beta_2 = 18.43°$ (denoted as S3)-are introduced in the design of the stents

composed of square elements to verify the design theory. The thickness of the stents is $t_1 = 0.5$ mm, and the thickness of the crease is $t_2 = 0.25$ mm.

3. Simulation and theory results

To evaluate the folding performance of the designed crease, the simulation process was conducted by the software of the Origami Simulator. It is worth mentioning that to facilitate the folding process, we do not fabricate the structure into a cylindrical shape directly. Firstly, 2D sheets with creases structures are printed. Then the sheets are folded into a stent according to the crease pattern to an appropriate degree. The side openings of the folded stents are sealed by melted PLA, and finally, fold to the full construction state. The strain contours during the folding process of the stents R1, R2, S1, S2 and S3 with the maximum folding degree of 60%, 60%, 85%, 85% and 85% are shown in Fig. 5, respectively.

During the folding process, all of the deformations of creases are set to be synchronized. When the folding degree reaches 30%−45%, the 2D sheets are rolled up into cylinders, and the stents can be obtained. As the folding process continued, the volume of the stents gradually decrease. It can be seen that when the folding degree reaches 60% and 85%, the volume of the stents shrinks to a fairly small scale. The simulation results indicate that following the pre-designed creases pattern, the stents can be successfully folded.

R_{o1} and R_{o2} are the key parameters that determine the shrinkage ratio of the stents. According to the geometry relation, during the folding
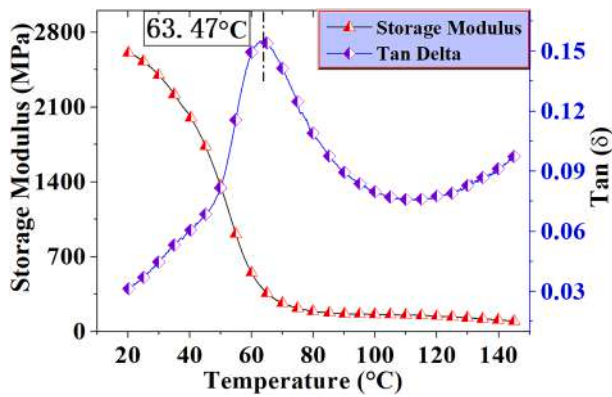
Fig. 7. Storage modulus and tan (δ) curves of the shape-memory PLA.

process, θ changes gradually, and it satisfies $\theta \in \left[\delta, \frac{\pi}{2}\right]$. The theoretical results of R_{o1} and R_{o2} changing with θ during the folding process are shown in Fig. 6. When $\theta \rightarrow 0$, R_{o1} gradually tends to the maximum value. The smaller the value of α_1, the larger the value of R_{o1}. Obviously, the value of R_{o1} with $\alpha_1 = \frac{\pi}{4}$ is larger than that with $\alpha_1 = \frac{\pi}{3}$ as shown in Fig. 6 (a) and (b). In the second step, the angle θ gradually decreases in the folding process. For δ with same value, its trend is the same. Fig. 6 (c) illustrates the variation of R_{o2} with $\alpha_1 = \frac{\pi}{4}$ changing with θ.

4. Materials and methods

4.1. Fabrication of stents by 4D printing

All the stents were fabricated using a commercial printer (ANYCUBIC 3D i3 MEGA) with a 0.4 mm diameter nozzle. The shape-memory polylactic acid (shape-memory PLA) filament fed to the printer was prepared using a twin-screw extruder (Cte20 Coperion) equipped with a sharp-shearing extruder screw. The screw speed was set as 200 rpm, and the processing temperature range was 180–200 °C. The diameter of the extruded filament was approximately 1.75 mm. The printing speed was set as 30 mm/min. The extrusion temperature was 190 °C, and the build-plate temperature was 60 °C. The sheet structures programmed crease patterns were first printed and then folded the sheets following the predesigned creases. To facilitate the operation, the two ends of the sheets are bonded by melted shape-memory PLA together when the structures were folded to about 40%. After the two ends of the pieces are glued together, proceed to complete the remaining folds process.

4.2. Material and experiments

The dynamic mechanical properties of shape-memory PLA were analyzed using DMA (Mettler Toledo, DMA/SDTA861e, Switzerland). The tensile mode was selected in the experiment, with a loading frequency of 1 Hz. The dimensions of the sample were 20 mm × 3.5 mm × 0.2 mm, and the test temperature ranged from 0 °C to 145 °C, with a heating rate of 5 °C/min.

Thermomechanical cycling experiments were performed using a ZWICK 010 (Zwick/Roell, Germany) universal testing machine. The sample followed the ASTM D638 standard (Type IV) and had dimensions of 115 mm × 6 mm × 3 mm. Firstly, a preload of 0.5 N was applied to the sample with a loading rate of 1 mm/min. Secondly, the specimen was heated to 90 °C with a heating rate of 2 °C/min. Subsequently, a 5 mm deformation was applied to the sample with a loading rate of 2 mm/min. Then the temperature was reduced to 20 °C at a cooling rate of 2 °C/min while the deformation was kept constant. Finally, the sample was
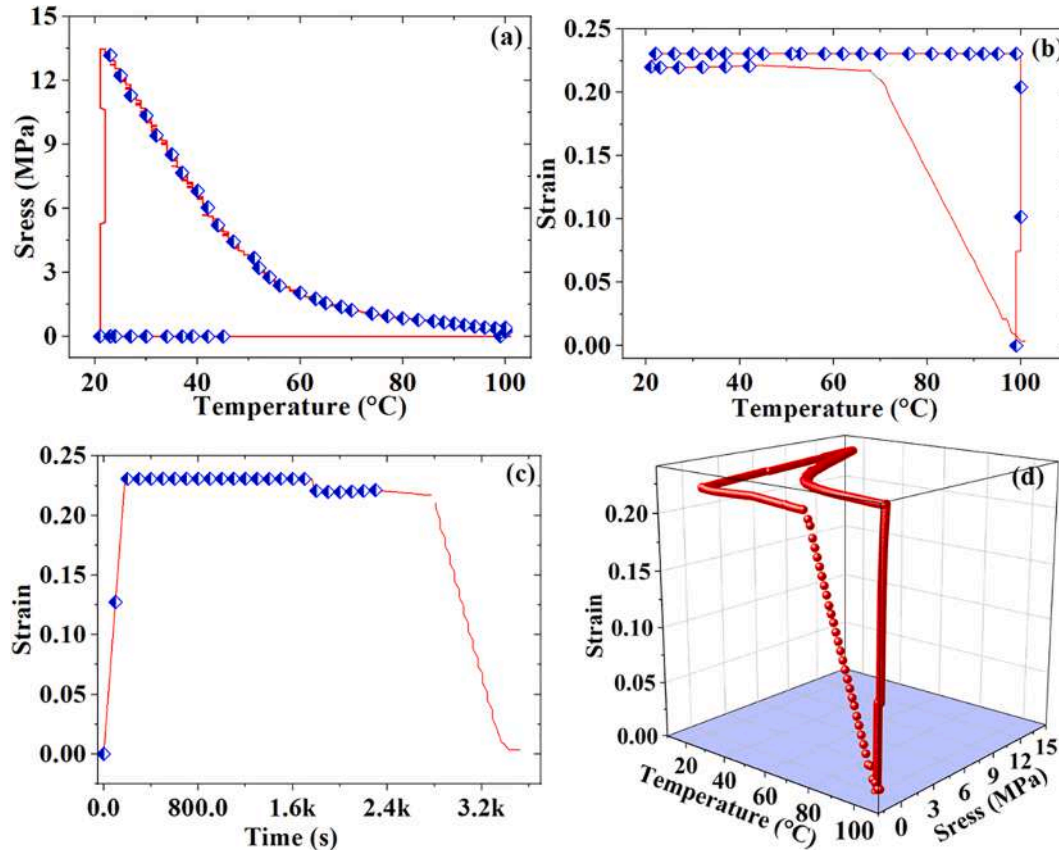

Fig. 8. Shape memory behavior characterization: (a) stress vs. temperature (b) strain vs. temperature (c) strain vs. time (d) relationship between the strain, stress and temperature.
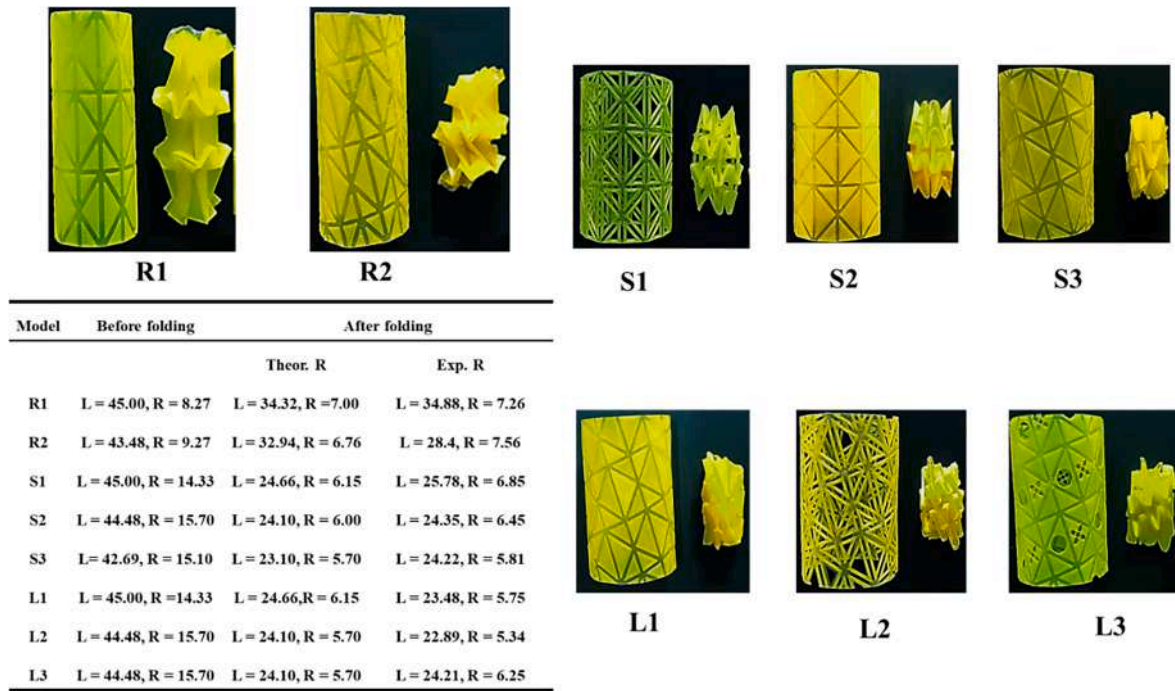
Model	Before folding	After folding	
		Theor. R	Exp. R
R1	L = 45.00, R = 8.27	L = 34.32, R =7.00	L = 34.88, R = 7.26
R2	L = 43.48, R = 9.27	L = 32.94, R = 6.76	L = 28.4, R = 7.56
S1	L = 45.00, R = 14.33	L = 24.66, R = 6.15	L = 25.78, R = 6.85
S2	L = 44.48, R = 15.70	L = 24.10, R = 6.00	L = 24.35, R = 6.45
S3	L= 42.69, R = 15.10	L = 23.10, R = 5.70	L = 24.22, R = 5.81
L1	L = 45.00, R =14.33	L = 24.66,R = 6.15	L = 23.48, R = 5.75
L2	L = 44.48, R = 15.70	L = 24.10, R = 5.70	L = 22.89, R = 5.34
L3	L = 44.48, R = 15.70	L = 24.10, R = 5.70	L = 24.21, R = 6.25

Fig. 9. Stents prepared via 4D printing before and after folding; Geometric parameters of the stents before and after folding obtained from the theory and experiment (Theor. R: Theoretical results after folding, Exp. R: Experimental results after folding).
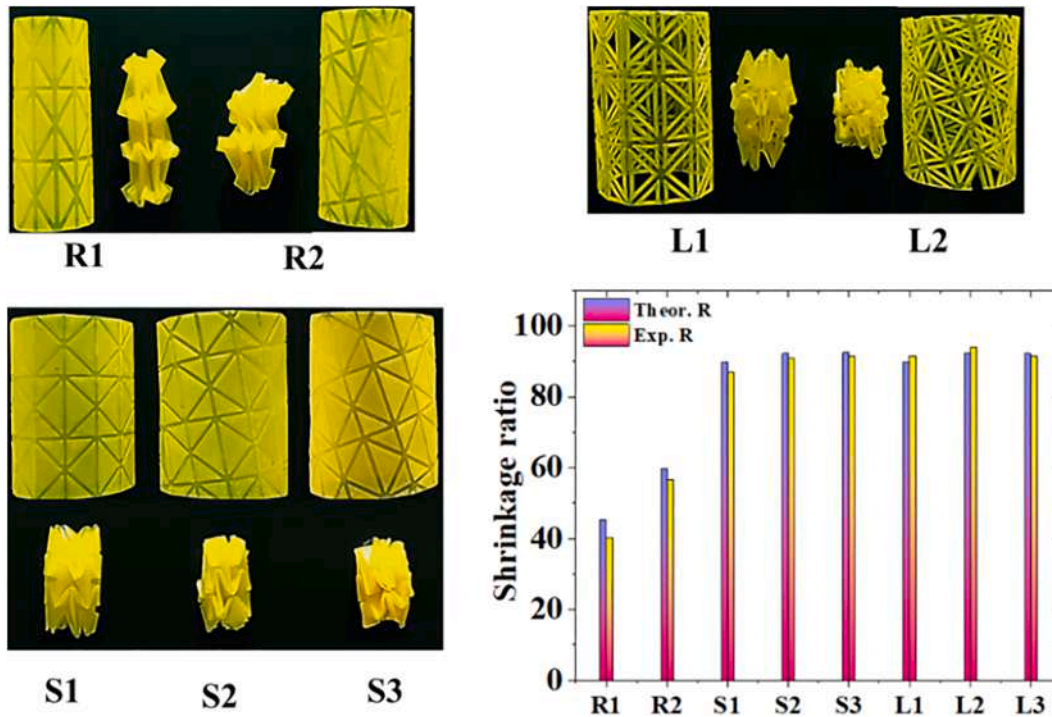

Fig. 10. Comparison of stents before and after folding (Theor. R: Theoretical results after folding, Exp. R: Experimental results after folding).

unloaded and reheated to 100 °C at a heating rate of 2 °C/min. The changes in the stress and strain with respect to the temperature were recorded.

Compression experiments and three-point bending experiments were conducted to investigate the mechanical properties of the self-assembly stents. The test temperature was 37 °C with a loading rate of 5 mm/min using a ZWICK 010 universal testing machine.

5. Results and discussions

5.1. Thermal properties of SMP

The storage modulus of shape memory PLA was 2.4 GPa at room temperature (25 °C) as shown in Fig. 7. However, with the increase of the temperature, the storage modulus rapidly decreased, reaching 425 MPa at 60 °C. Moreover, the loss angle-temperature curve showed that
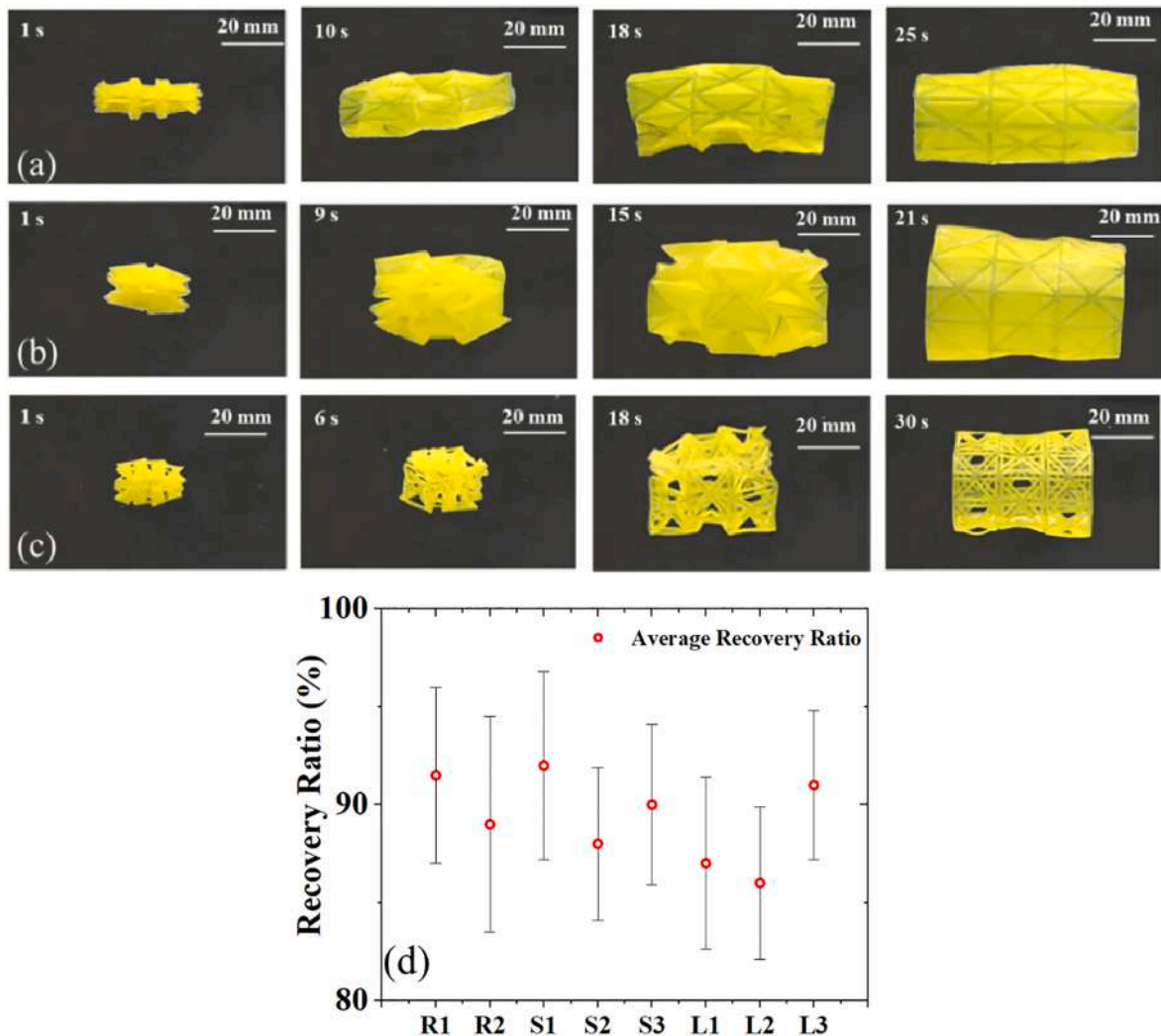
Fig. 11. Self-assembly process of the stents (a) R1 (b) S1 (c) L1 (d) Recovery ratio of stents.

the shape-memory PLA had a wide transition-temperature range of 45 °C to 80 °C, and the peak value was 63.47 °C. Consequently, the structure can finish its self-assembly process within this temperature range.

The thermomechanical cycling experiment characterized the relationship between temperature, time, stress and strain, as shown in Fig. 8. When the temperature was 100 °C, the shape-memory PLA was in the rubbery state. The stress of the structure was close to zero during the loading process, as shown in Fig. 8(a). However, the PLA completed the transition process from a rubbery state to a glassy state with the decrease of the temperature, and the stress gradually increased from 0.4 MPa to 13.4 MPa. As depicted in Fig. 8(b), the sample started to recover the shape in memory when the temperature was approximately 62 °C. The sample completed the shape-memory process when the temperature was 100 °C, and the shape-recovery ratio was 98%. However, owing to the hysteresis of the heating process, the recovery phenomenon should have occurred at approximately 55 °C. Fig. 8(c) presented the change in the strain over time, and it can be obtained that the shape fixity ratio was up to 98%. The relationship between stress, strain, and the temperature was illustrated in Fig. 8(d). The shape-memory behavior characterization indirectly reflected the self-assembly process of the stent.

5.2. Variation of geometrical parameters before and after folding

The configurations of the stents before and after folding were shown

in Fig. 9. According to the theoretical model (Supporting Information S1 and S2), we calculated the theoretical value of the size of the stents after folding and compared it with the experiments as shown in the table. After these structures were folded along the predesigned creases, the volume of the stent in the contracted state was significantly reduced compared with that before folding. The stents R1 and R2 were composed of rectangular elements, and others are composed of square elements as shown in Fig. 9. No fracture or damage occurred during the folding process.

Using the statistical results, the shrinkage ratio of the stents was calculated using the following formula.

$$S = \frac{O - F}{O} \times 100\% \tag{7}$$

where S represents the shrinkage ratio, O represents the original dimension, and F represents the folded dimension.

The shrinkage ratios obtained from the experiments were slightly lower than the theoretical values. This can be attributed to the fact that the theoretical value was obtained under the assumption that all the elements behave identically during folding; the mismatch between each unit was not taken into account. The effect of creases on the shrinkage ratio cannot be ignored. However, there were exceptions, such as the shrinkage ratio of the stents after the introduction of the lightweight design, which was slightly higher than the theoretical value. This result is reasonable because the material at the crease was hollow, making the
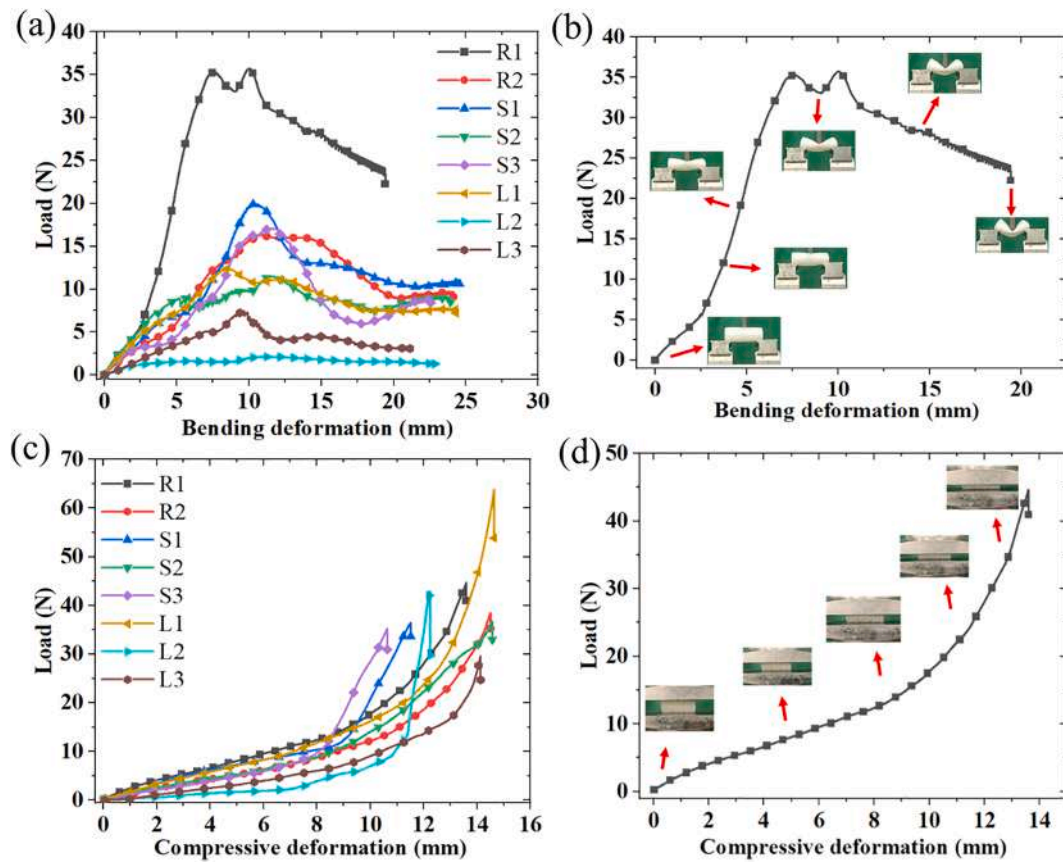
Fig. 12. Mechanical properties of the self-assembly stents (a) Three-point bending test (b) Configuration of stent R1 changing with load (c) Radial strength test (d) Configuration of stent R1 changing with the compressive load.

structure more flexible and the deformation more harmonious.

The shrinkage ratio of a stent composed of rectangular elements was minimal, and the theoretical folded volume was 54.6% of the original volume. Owing to the uncoordinated deformation of rectangular elements during the folding process, the actual volume obtained from the experiment was 59.7% of the original volume. However, for the stent after the introduction of a helical angle, the shrinkage ratio increased significantly, and the volume of folded stent obtained from the experiment was 40.3% of the initial volume. Moreover, stents composed of square elements have superior deformation coordination, resulting in increased shrinkage ratios. For the structure without a helical angle, the shrinkage ratio was 86.9%.

As the theory predicts, the obtained shrinkage ratio increased with the helical angle. For example, the shrinkage ratio was 90.8% for the stent with a helical angle of $\beta_1 = 8.6°$ and 91.6% for the stent with a helical angle of $\beta_2 = 18.43°$. By introducing the lightweight design, the flexibility of the structure was increased. The shrinkage ratio of the stent without a helical angle was 91.6%, which was higher than the theoretical value of 89.9%. The shrinkage ratio of stent L2 after the introduction of the helical angle increased to 94%. However, for structure L3, because there was no lightweight design for its creases, the shrinkage ratio was 91.4%.

To examine the influence of the introduction of the helical angle on the shrinkage ratio of the stents, the structures before and after folding and with and without the helical angle were compared, as depicted in Fig. 10. With the introduction of the helical angle, the structures contracted further along the length. The larger the helical angle, the greater the contraction degree, which can be seen visually from the before and after folding state and the shrinking ratio graph.

5.3. Self-assembly

The origami concept provides innovative solutions for compressing large objects into small spaces. It has been widely used in many applications, including cartons, shopping bags, photovoltaic solar panels, and car airbags. These products produced via traditional technology cannot deploy automatically once they are folded, making it difficult to employ them for self-assembly applications in operating environments where manual reconfiguration is difficult. However, the origami-derived stents fabricated via 4D printing can be implanted into the body in a compaction state and finish its self-assembly process utilizing the shape memory effect of SMP, which greatly facilitates the operation of minimally invasive surgery.

Because the transformation temperature ranged from 45 °C to 80 °C, the self-assembly function of the stents was evaluated in a 60 °C water bath. The structure was gradually deployed stimulated by the temperature via the unique driving mechanism of the SMP. The self-assembly process of the stents R1, S2 and S3 were illustrated in Fig. 11(a), (b) and (c), respectively. Stents S1, S2 and S3 recovered to their initial state within 25 s, 20 s, 30 s, respectively.

Although the introduction of the lightweight design changed the configuration of the unit cell, the self-assembly process was not significantly affected. The self-assembly process of R2, S2, S3, L2 and L3 can be found in Supporting Information, Fig. S12. Moreover, because the crease played the role of a soft hinge, providing the driving force for self-assembly, the geometric parameters of the hinge could be adjusted by optimizing the material distribution at the crease to regulate structural flexibility. Fig. 11(d) illustrated the recovery ratio of stents, and it can be seen that the average recovery ratios of the eight stents were higher than 85%. The highest recovery ratios were up to 97%.

5.4. Characterization of mechanical properties

The stent will be subject to complex loading in vivo, the main role is to restore and maintain the lumen patency. The stents should have stable mechanical properties, both strength and flexibility, providing support for softened or damaged tissues and adapting to cavity deformation. Consequently, the radial support strength and the flexible performance are the two essential criteria for stents. To investigate the mechanical properties, stents with a diameter of 18 mm were prepared according to the size of the pig trachea. The thickness of the stents is $t_1 = 1$ mm, and the thickness of the crease is $t_2 = 0.5$ mm.

The bending properties and radical strengths were illustrated in Fig. 12. As shown in Fig. 12(a), the bending property of the stents after the lightweight design is better than the first five stents. The bending strength of stent R1 is the highest while stent L2 is the lowest. Furthermore, it can be concluded that neither the configuration of creases nor the helix angle has much influence on the bending resistance of stents. The configuration of the stents from loading to failure changing with load is shown in Fig. 12(b) and Supporting Information, Fig. S13. From the compression test results (Fig. 12(c)), it can be seen that the compression performance of these stents differs little. Furthermore, the load of the stents composed of the lightweight elements was slightly smaller than the other groups. The configuration of creases nor the helix angle has much influence on the radial strength of stents. The configuration change of the stents under compressive load is shown in Fig. 12(d) and Supporting Information, Fig. S14.

6. Conclusions

In this work, stents with self-assembly functions that derived from the origami concept were proposed and fabricated by 4D printing. The shrinkage ratios of stents with different unit cells and helical angles were calculated theoretically and verified experimentally, which was ranging from 40.3% to 94%. By introducing helical angles into the structure, the shrinkage ratio of the stents is further improved. Additionally, the introduction of a lightweight design reduces the amount of material used, changes the configuration of the flexure hinge, increases the structural flexibility, and further increases the shrinkage ratio. A comparison between the initial and folded states of the stent, as well as the demonstration of self-assembly stimulated by heat, highlights the potential applications of self-assembly stents in tissue engineering. Combining the origami concept with 4D printing and extending the design concept to the 3D space signifies more exploration possibilities.

Declaration of Competing Interest

The authors declare that they have no known competing financial interests or personal relationships that could have appeared to influence the work reported in this paper.

Acknowledgements

Appendix A. Supplementary material

Supplementary data to this article can be found online at https://doi.org/10.1016/j.compstruct.2022.115669.

References

[1] Zarek M, Mansour N, Shapira S, Cohn D. 4D printing of shape memory-based personalized endoluminal medical devices. Macromol Rapid Comm 2017;38(2): 1600628.

[2] Sun ZH, Jansen S. Personalized 3D printed coronary models in coronary stenting. Quant Imag Med Surd 2019;9(8):1356–67.

[3] Meloni M, Cai JG, Zhang Q, Lee DSH, Li M, Ma RJ, et al. Engineering origami: a comprehensive review of recent applications, design methods, and tools. Adv Sci 2021;8(13):2000636.

[4] Liu Z, Fang H, Xu J, Wang KW. A novel origami mechanical metamaterial based on Miura-variant designs: exceptional multistability and shape reconfigurability. Smart Mater Struct 2021;30(8):085029.

[5] Zhang Q, Fang H, Xu J. Programmable stopbands and supra transmission effects in a stacked Miura-origami metastructure. Phys Rev E 2020;101(4):042206.

[6] Tao R, Ji L, Li Y, Wan Z, Hu W, Wu W, et al. 4D printed origami metamaterials with tunable compression twist behavior and stress-strain curves. Compos Part B-Eng 2020;201:108344.

[7] Xin XZ, Liu LW, Liu YJ, Leng JS. Origami-inspired self-deployment 4D printed honeycomb sandwich structure with large shape transformation. Smart Mater Struct 2020;29(6):65015.

[8] Resch RD. The topological design of sculptural and architectural systems. In: Nat Comp Conf and Exp., vol. 4, no. 8. New York: ACM; 1973. p. 643–50.

[9] Resch RD, Christiansen H. The design and analysis of kinematic folded plate systems. Proceedings of IASS Symposium on Folded Plates and Prismatic Structures, Vienna. 1970.

[10] Lv C, Krishnaraju D, Konjevod G, Yu H, Jiang H. Origami based Mechanical Metamaterials. Sci Rep 2015;4(1).

[11] Tomohiro T. Designing freeform origami tessellations by generalizing resch's patterns. J Mech Des 2013;135:111006.

[12] Qiu C, Zhang K, Dai JS. Repelling-screw based force analysis of origami mechanisms. J Mech Robot 2016;8(3):031001.

[13] Chen Y, Feng HJ, Ma JY, Peng R, You Z. Symmetric waterbomb origami. Proc Roy Soc A Math Phys Eng Sci 2016;472(2190):20150846.

[14] Bowen L, Springsteen K, Feldstein H, Frecker M, Simpson TW, Von Lockette P. Development and validation of a dynamic model of magnetoactive elastomer actuation of the origami waterbomb base. J Mech Robot 2015;7(1):011010.

[15] Felton S, Tolley M, Demaine E, Rus D, Wood R. A method for building self-folding machines. Science 2014;345(6197):644–6.

[16] Zhao W, Liu LW, Zhang FH, Leng JS, Liu YJ. Shape memory polymers and their composites in biomedical applications. Mat Sci Eng C-Mater 2019;97:864–83.

[17] Zhao W, Zhang F, Leng J, Liu Y. Personalized 4D printing of bioinspired tracheal scaffold concept based on magnetic stimulated shape memory composites. Compos Sci Technol 2019;184:107866.

[18] Zhang W, Wang H, Wang HT, Chan John YE, Liu HL, Zhang B, et al. Structural multi-colour invisible inks with submicron 4D printing of shape memory polymers. Nat Commun 2021;12(1):1–8.

[19] Zhao W, Zhu J, Liu L, Leng J, Liu Y. Analysis of small-scale topology and macroscale mechanical properties of shape memory chiral-lattice metamaterials. Compos Struct 2021;262:113569.

[20] MaoYQ CF, Hou SJ, Qi HJ, Yu K. A viscoelastic model for hydrothermal activated malleable covalent network polymer and its application in shape memory analysis. J Mech Phys Solids 2019;127:239–65.

[21] Chen L, Zhang Y, Ye HT, Duan GH, Duan HG, Ge Q, et al. Color-changeable four-dimensional printing enabled with ultraviolet-curable and thermochromic shape memory polymers. ACS Appl Mater Inter 2021;13(15):18120–7.

[22] Montgomery SM, Kuang X, Armstrong CD, Qi HJ. Recent advances in additive manufacturing of active mechanical metamaterials. Curr Opin Solid St M 2020;24 (5):100869.

[23] Wang H, Fang L, Zhang Z, Epaarachchi J, Li L, Hu X, et al. Light-induced rare earth organic complex/shape-memory polymer composites with high strength and luminescence based on hydrogen bonding. Compos Part A-Appl 2019;125:105525.

[24] Urbina L, Alonso-Varona A, Saralegi A, Palomares T, Eceiza A, Corcuera M, et al. Hybrid and biocompatible cellulose/polyurethane nanocomposites with water-activated shape memory properties. Carbohyd Polym 2019;216(15):86–96.

[25] Zhao W, Huang Z, Liu L, Wang W, Leng J, Liu Y. Porous bone tissue scaffold concept based on shape memory PLA/Fe$_3$O$_4$. Compos Sci Technol 2021;203: 108563.

[26] Bajpai A, Baigent A, Raghav S, Bradaigh CO, Koutsos V, Radacsi N. 4D Printing: materials, technologies, and future applications in the biomedical field. Sustainability 2020;12(24):10628.

[27] Melocchi A, Uboldi M, Cerea M, Cerea M, Foppoli A, Maroni A, et al. Shape memory materials and 4D printing in pharmaceutics. Adv Drug Deliver Rev 2021; 173:216–37.

[28] Ramaraju H, Akman RE, Safranski DL, Hollister SJ. Designing biodegradable shape memory polymers for tissue repair. Adv Funct Mater 2020;30(44):2002014.

[29] Peraza-Hernandez EA, Hartl DJ, Malak Jr RJ, Lagoudas DC. Origami-inspired active structures: a synthesis and review. Smart Mater Struct 2014;23(9):094001.

[30] Randall CL, Gultepe E, Gracias DH. Self-folding devices and materials for biomedical applications. Trends Biotechnol 2012;30(3):138–46.

[31] Bolaños Quiñones VA, Zhu H, Solovev AA, Mei Y, Gracias DH. Origami biosystems: 3D assembly methods for biomedical applications. Adv Biol 2018;2(12):1800230.

[32] Lazarus N, Smith GL, Dickey MD. Self-folding metal origami. Adv Intell Syst 2019;1 (7):1900059.

[33] Ge Q, Dunn CK, Qi HJ, Dunn ML. Active origami by 4D printing. Smart Mater Struct 2014;23(9):094007.

[34] Bobbert FSL, Janbaz S, van Manen T, Li Y, Zadpoor AA. Russian doll deployable meta-implants Fusion of kirigami, origami, and multi-stability. Mater Des 2020; 191:108624.

[35] Banerjee H, Li TK, Ponraj G, Kirthika SK, Lim CM, Ren HL. Origami-layer-jamming deployable surgical retractor with variable stiffness and tactile sensing. J Mech Rob 2020;12:031010.

[36] Sargent B, Butler J, Seymour K, Bailey D, Jensen B, Magleby S, et al. An origami-based medical support system to mitigate flexible shaft buckling. J Mech Rob 2020; 12:041005.

[37] Felton S, Tolley M, Demaine E, Rus D, Wood R. A method for building self-folding machine. Science 2014;345(6197):644–6.

[38] Teoh JM, An J, Feng X, Zhao Y, Chua CK, Liu Y. Design and 4D printing of cross folded origami structures: a preliminary investigation. Materials 2018;11(3):376.

[39] Liu Y, Boyles JK, Genzer J, Dickey MD. Self-folding of polymer sheets using local light absorption. Soft Matter 2012;8(6):81764–9.

[40] Tolley MT, Felton SM, Miyashita S, Aukes D, Rus D, Wood RJ. Self-folding origami: shape memory composites activated by uniform heating. Smart Mater Struct 2014; 23(9):094006.